LETTERS
https://doi.org/10.1038/s41558-019-0552-3
nature climate change

Enhanced oceanic CO_2 uptake along the rapidly changing West Antarctic Peninsula

Michael S. Brown[1*], David R. Munro[2,6,7], Colette J. Feehan[3], Colm Sweeney[4], Hugh W. Ducklow[5] and Oscar M. Schofield[1]

The global ocean is an important sink for anthropogenic CO_2 (ref. [1]). Nearly half of the oceanic CO_2 uptake occurs in the Southern Ocean[2]. Although the role of the Southern Ocean CO_2 sink in the global carbon cycle is recognized, there are uncertainties regarding its contemporary trend[3,4], with a need for improved mechanistic understanding, especially in productive Antarctic coastal regions experiencing substantial changes in temperature and sea ice[5]. Here, we demonstrate strong coupling between summer upper ocean stability, phytoplankton dynamics and oceanic CO_2 uptake along the rapidly changing West Antarctic Peninsula using a 25-year dataset (1993–2017). Greater upper ocean stability drives enhanced biological production and biological dissolved inorganic carbon drawdown, resulting in greater oceanic CO_2 uptake. Diatoms achieve higher biomass, oceanic CO_2 uptake and uptake efficiency than other phytoplankton. Over the past 25 years, changes in sea ice dynamics have driven an increase in upper ocean stability, phytoplankton biomass and biological dissolved inorganic carbon drawdown, resulting in a nearly fivefold increase in summer oceanic CO_2 uptake. We hypothesize that continued warming and declines in sea ice will lead to a decrease in biological dissolved inorganic carbon drawdown, negatively impacting summer oceanic CO_2 uptake. These results from the West Antarctic Peninsula provide a framework to understand how oceanic CO_2 uptake in other Antarctic coastal regions may be altered due to climate change.

The global ocean is an important CO_2 sink given its ability to absorb and sequester atmospheric CO_2. The air–sea CO_2 flux is proportional to the difference between the partial pressure of CO_2 in the surface ocean ($p_{CO_{2,sur}}$) and atmosphere ($p_{CO_{2,atm}}$), that is Δp_{CO_2}, where a negative (positive) Δp_{CO_2} indicates a flux of CO_2 to the ocean (atmosphere)[6]. Typically, $p_{CO_{2,sur}}$ is more variable than $p_{CO_{2,atm}}$, and thus Δp_{CO_2} is primarily controlled by $p_{CO_{2,sur}}$ (ref. [6]). Variability in $p_{CO_{2,sur}}$ is controlled by temperature, salinity, dissolved inorganic carbon (DIC) and total alkalinity (TA), with DIC and TA affected by biological production, anthropogenic CO_2, mixing and circulation[3]. The air–sea CO_2 flux is also dependent on the air–sea CO_2 transfer velocity, which is parameterized with wind speed[6]. Given that over our study period there is no long-term trend in wind speed during summer along the West Antarctic Peninsula (WAP)[7], and due to uncertainty in both wind speed estimates and the transfer velocity parameterization, here we use Δp_{CO_2} to assess variability in oceanic CO_2 uptake, consistent with previous studies[8–10].

The WAP marine ecosystem (Fig. 1) is undergoing substantial physical changes[5]. Atmospheric temperatures are warming rapidly, including a 7 °C increase in winter surface temperatures since 1950 (five times the global average)[11]. Additionally, there have been long-term increases in oceanic temperatures[12,13], a majority of marine glaciers are in retreat[14], and since 1979 the sea ice season has shortened by 3 months[15]. These changes are associated with strengthening winds over the Southern Ocean[16], driven by large-scale climate variability, including a positive trend in the Southern Annular Mode (SAM)[17], and co-variability between the SAM and the El Niño/Southern Oscillation[18]. Due to the north–south orientation of the WAP, there are meridional differences in warming, glacial retreat and sea ice decline[19]. Along the northern WAP, maritime conditions have progressed southward, where warming and strong winds have led to a substantial long-term decline in sea ice, resulting in decreased upper ocean stability[20]. Polar conditions persist along the mid/southern WAP (our focus here), although warming and wind-driven advection has led to increased inter-annual variability and a smaller long-term decline in sea ice[7,15,21]. Given that Antarctic marine organisms are dependent on sea ice dynamics, these physical changes along the WAP have resulted in alterations to the marine food web across all trophic levels[5].

The WAP marine ecosystem is highly productive and characterized by large coastal phytoplankton blooms during spring and summer[19]. Given that macronutrients are abundant[22], it has been hypothesized that biological production along the WAP is primarily controlled by light availability, which is a function of upper ocean stability[7,23–25]. However, micronutrients like iron may be limiting on the shelf and slope[26,27]. It has also been demonstrated that biological production can drive variability in oceanic CO_2 uptake along the WAP[28–33]. These previous studies have been limited in spatio-temporal extent and/or with minimal focus on the role of phytoplankton community composition. Here, we investigate the coupling between upper ocean stability, phytoplankton dynamics (biomass and composition) and oceanic CO_2 uptake during summer along the mid/southern WAP over a 25-year period (1993–2017), using data collected by the Palmer Long-Term Ecological Research (LTER) and Drake Passage Time-Series (DPT) programmes.

[1]Center for Ocean Observing Leadership, Department of Marine and Coastal Sciences, Rutgers University, New Brunswick, NJ, USA. [2]Department of Atmospheric and Oceanic Sciences, and Institute of Arctic and Alpine Research, University of Colorado, Boulder, CO, USA. [3]Department of Biology, Montclair State University, Montclair, NJ, USA. [4]Global Monitoring Division, Earth System Research Laboratory, National Oceanic and Atmospheric Administration, Boulder, CO, USA. [5]Lamont-Doherty Earth Observatory, Columbia University, Palisades, NY, USA. [6]Present address: Cooperative Institute for Research in Environmental Sciences, University of Colorado, Boulder, Colorado, USA. [7]Present address: Global Monitoring Division, Earth System Research Laboratory, National Oceanic and Atmospheric Administration, Boulder, CO, USA. *e-mail: mbrown@marine.rutgers.edu

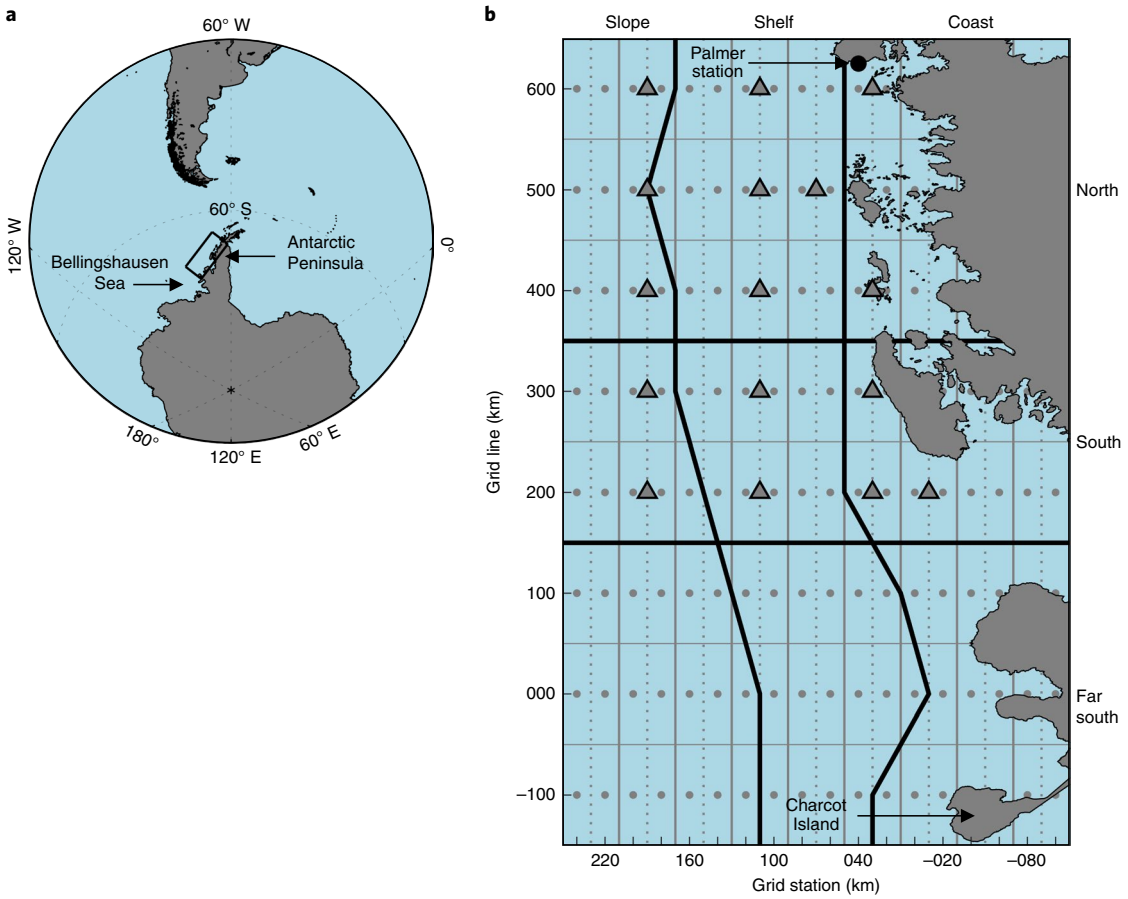

Fig. 1 | Study area. a, The Southern Ocean and Antarctic continent. **b**, Enlargement of the Palmer LTER regional sampling grid (boxed region in **a**) along the mid/southern WAP. The grey dots and grey dotted lines indicate individual sampling stations and their borders, respectively. The grey solid lines indicate groups of two sampling stations. The black solid lines indicate the subregions of the Palmer LTER regional sampling grid, including the north to far south and slope to coast. Groups of two sampling stations encompassing stations that are typically visited each year are marked with grey triangles, and were used for the regional and subregional time series. The grid lines/stations are numbered relative to a location in the far south/coast.

An inverse relationship between chlorophyll-*a* (chl-*a*) and Δp_{CO_2} indicates the critical role of biological production in driving oceanic CO_2 uptake. Surface averages of chl-*a* via fluorescence and Δp_{CO_2} were calculated at the Palmer LTER regional sampling grid stations (Fig. 1b; see Methods). In general, Δp_{CO_2} is negative (Fig. 2a). There is a significant negative correlation between chl-*a* and Δp_{CO_2} (Spearman's rho, $r_s = -0.62$, $P < 0.001$; Fig. 2a). Climatological chl-*a* (Δp_{CO_2}) shows a cross-shore gradient, with higher (lower) values towards the coast (Fig. 2b,c). There is a significant negative correlation between yearly subregional (slope, shelf and coast subregions) chl-*a* and Δp_{CO_2} ($r_s = -0.53$, $P = 0.008$; $r_s = -0.60$, $P = 0.002$; $r_s = -0.64$, $P < 0.001$, respectively; Fig. 2d). Summer surface warming (freshening) can also increase (decrease) Δp_{CO_2}, although these effects typically offset each other and cannot account for the large variability observed in Δp_{CO_2} (Fig. 2a)[29]. These results demonstrate that during summer along the mid/southern WAP, the region is a strong sink for CO_2, and biological production is a primary driver of oceanic CO_2 uptake.

To assess the extent to which upper ocean stability is a primary control on biological production, mixed-layer depth (MLD) was determined from CTD (conductivity–temperature–depth instrument) casts and surface averages of chl-*a* via high-performance liquid chromatography (HPLC) were calculated at the Palmer LTER regional sampling grid stations (Fig. 1b; see Methods). Along the WAP, MLD is controlled by wind, sea ice and meltwater dynamics, which are driven by large-scale climate variability. During negative SAM/El Niño conditions, cold and weak southerly winds blow across the region, resulting in high sea ice concentrations that reduce wind-mixing in winter and supply meltwater in spring/summer, which along with glacial meltwater stabilizes the upper ocean, supporting large phytoplankton blooms[7,15,18–21,23–25]. The opposite occurs during positive SAM/La Niña conditions. Climatological MLD shows a meridional and cross-shore gradient, with deeper MLDs further north and offshore (Supplementary Fig. 1). Higher chl-*a* concentrations are primarily associated with shallower MLDs (Fig. 3), where phytoplankton cells are retained in the upper ocean, reducing light limitation. This supports the hypothesis that during summer along the mid/southern WAP, upper ocean stability is a primary control on biological production. Lower Δp_{CO_2} values are primarily associated with higher chl-*a* concentrations at shallower MLDs (Fig. 3). The positive monotonic relationship between Δp_{CO_2} and MLD (Fig. 3) demonstrates that MLD can also drive variability in Δp_{CO_2} independent of biological production. Modelling Δp_{CO_2} as a function of MLD with constant biological production (see Methods) indicates that shallower MLDs drive lower Δp_{CO_2} values due to higher biological volumetric DIC drawdown (Fig. 3). These results demonstrate that during summer along the mid/southern WAP, there is strong coupling between upper ocean physics and biogeochemistry, in which greater upper ocean stability drives enhanced biological DIC drawdown (through both enhanced biological production and

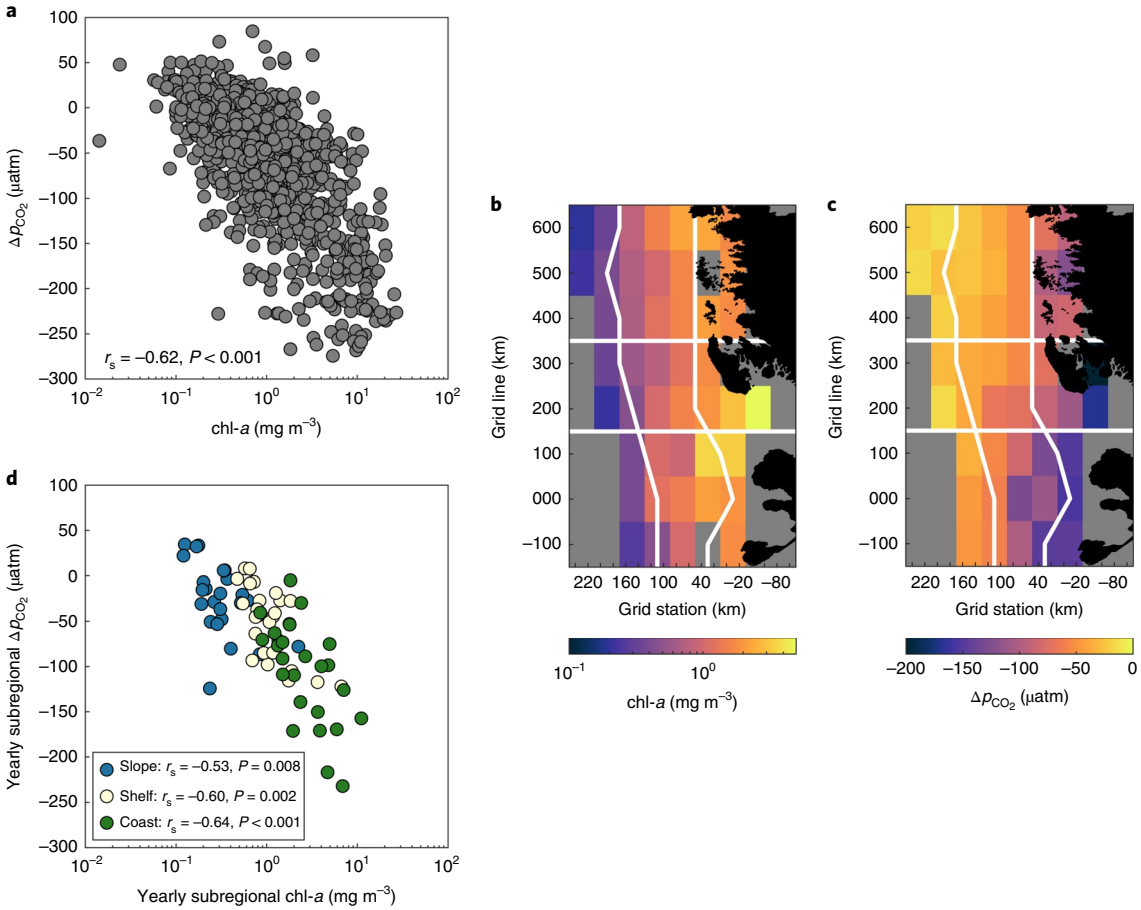

Fig. 2 | Relationship between summer WAP phytoplankton biomass and oceanic CO_2 uptake. a, Scatter plot of Δp_{CO_2} versus chl-*a* via fluorescence. **b**,**c**, Climatologies of chl-*a* (**b**) and Δp_{CO_2} (**c**). **d**, Scatter plot of yearly subregional (Fig. 1b) Δp_{CO_2} versus chl-*a*. In **a** and **d**, $n = 1151$ and 25, respectively.

biological volumetric DIC drawdown), resulting in greater oceanic CO_2 uptake.

The importance of phytoplankton community composition, determined with CHEMTAX using accessory pigments via HPLC (see Methods), on phytoplankton biomass and oceanic CO_2 uptake was also assessed. The primary regional phytoplankton groups are diatoms (typically large: >20 µm) and cryptophytes (small: <20 µm), although small dinoflagellates and unidentified phytoflagellates (that is 'mixed flagellates') can also contribute substantially to phytoplankton biomass[34]. At shallower MLDs, communities dominated (representing ≥50% of total chl-*a*) by diatoms (cryptophytes) are associated with lower (higher) Δp_{CO_2} values (Fig. 3). Communities dominated by mixed flagellates occur primarily at deeper MLDs, and are associated with higher Δp_{CO_2} values (Fig. 3). To examine differences in water mass properties (such as phytoplankton biomass, oceanic CO_2 uptake and uptake efficiency) between diatom, cryptophyte and mixed flagellate assemblages (representing ≥75% of total chl-*a*; Supplementary Fig. 2), Kruskal-Wallis tests were performed (see Methods). Diatoms, relative to cryptophytes, relative to mixed flagellates, achieve a significantly higher (lower) chl-*a* (Δp_{CO_2}) (Supplementary Fig. 3). Diatoms and cryptophytes occur at a similarly shallow MLD relative to mixed flagellates (Supplementary Fig. 4a). This allows for a direct comparison of the biogeochemical response of just diatoms and cryptophytes, since MLD influences biological volumetric DIC drawdown independent of biological production (Fig. 3). Diatoms occur in waters that are significantly lower in temperature than cryptophytes, but similar in salinity (Supplementary Fig. 4b,c). However, the resulting Δp_{CO_2} difference of 5 µatm due to temperature[6] cannot account for the lower Δp_{CO_2} of diatoms relative to cryptophytes. Diatoms also achieve a significantly lower salinity-normalized DIC, nitrate and phosphate than cryptophytes (Supplementary Fig. 5). These results demonstrate that during summer along the mid/southern WAP, diatoms achieve significantly higher biomass, oceanic CO_2 uptake and uptake efficiency than cryptophytes. The higher uptake efficiency of diatoms could be due to their larger size, their greater predation by krill[35], to cryptophyte mixotrophy[36] and/or to differences in micronutrient limitation, nutrient uptake ratios or growth rates.

Temporal trends during summer along the mid/southern WAP in regional and subregional (north and south subregions; Fig. 1b) upper ocean stability, phytoplankton dynamics and oceanic CO_2 uptake were determined using time series of MLD, chl-*a*, phytoplankton group chl-*a* and Δp_{CO_2} (see Methods; Supplementary Table 1). From 1993 to 2017, there was a significant decrease in regional MLD ($-1.3\,m\,yr^{-1}$, $P < 0.001$; Fig. 4a). This decrease in MLD is associated with a wind-driven increase since 2008 in sea ice[7,15,21] and declines since 1993 in upper ocean temperature, salinity and density due to continued sea ice melt, with minimal impact from variability in wind-driven mixing[7]. There was also a significant increase in regional chl-*a* via fluorescence ($+0.015\log_{10}[mg\,m^{-3}]\,yr^{-1}$, $P = 0.049$; Fig. 4b) and HPLC (Supplementary Table 1). This increase in regional chl-*a* is consistent with satellite observations[20] reporting a long-term increase (decrease) in chl-*a* along the mid/southern (northern) WAP. Additionally, subregional phytoplankton group chl-*a* trends indicate a large significant increase in diatoms relative to cryptophytes in the south subregion and a large significant

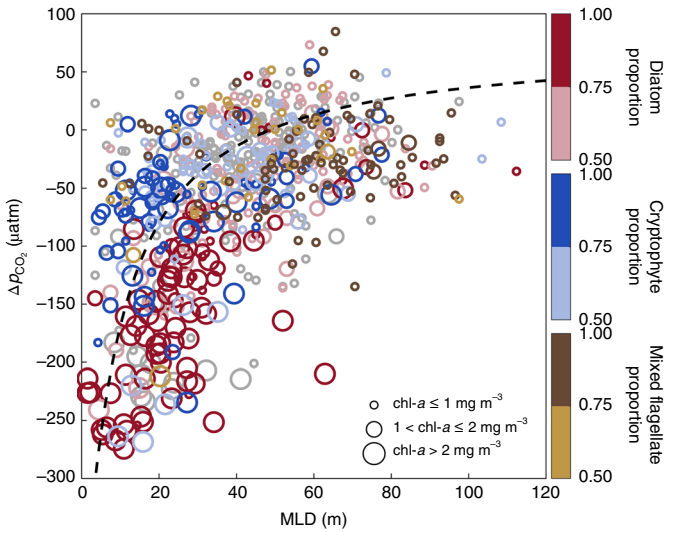

Fig. 3 | Relationship between summer WAP upper ocean stability, phytoplankton dynamics and oceanic CO_2 uptake. Symbol size indicates chl-*a* via HPLC. Symbol colour indicates diatom, cryptophyte, or mixed flagellate proportion (grey indicates that no group dominated, that is represented ≥50% of total chl-*a*). The black dashed line indicates Δp_{CO_2} modelled as a function of MLD with a constant rate of biological production (see Methods). $n = 702$.

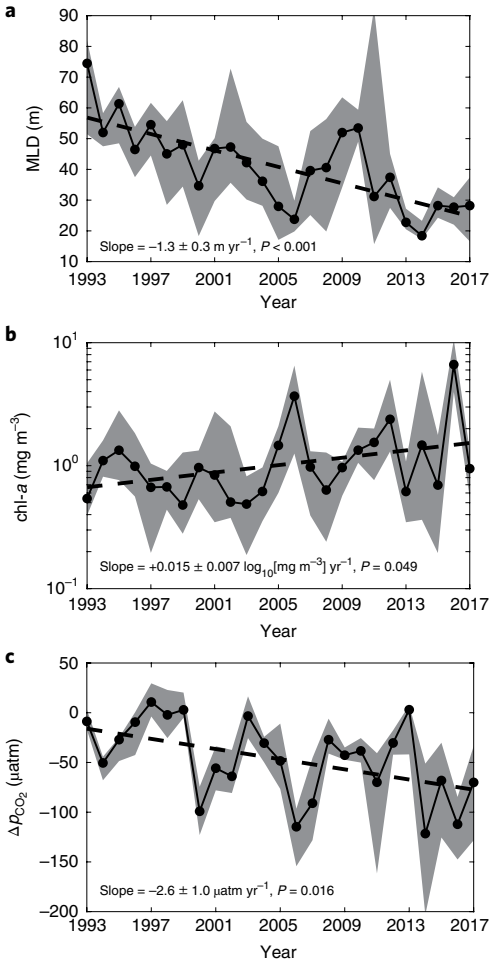

Fig. 4 | Trends in summer WAP regional upper ocean stability, phytoplankton biomass and oceanic CO_2 uptake. a–c, Time series of regional MLD (**a**), chl-*a* via fluorescence (**b**) and Δp_{CO_2} (**c**). The black solid lines and circles indicate yearly median values of observations at the Palmer LTER regional sampling grid stations that are typically visited each year (Fig. 1b; see Methods). The grey bands indicate the interquartile range. The black dashed lines indicate the linear temporal trend ($n = 25$).

increase in cryptophytes relative to diatoms in the north subregion (Supplementary Table 1). This meridional variability in subregional diatom and cryptophyte trends is also consistent with satellite observations[20] reporting a long-term increase (decrease) in diatom proportion along the mid/southern (northern) WAP. The significant regional increase in cryptophytes (Supplementary Table 1) also supports the hypothesis that this group will increase in abundance with continued meltwater inputs[34,37].

Consistent with the changes in regional MLD and chl-*a* (Fig. 4a,b), there was a significant decrease in regional Δp_{CO_2} (−2.6 µatm yr^{-1}, $P = 0.016$; Fig. 4c), representing a nearly fivefold increase in oceanic CO_2 uptake. Although this Δp_{CO_2} trend is similar in magnitude to the atmospheric CO_2 trend (1.9 ppm yr^{-1} at 65°S; Supplementary Fig. 6), an analysis of the $p_{CO_{2,sur}}$ trend drivers (see Methods; Supplementary Tables 1 and 2) demonstrates that the decrease in regional Δp_{CO_2} is due to offsetting effects on $p_{CO_{2,sur}}$ from increases in both biological DIC drawdown and anthropogenic DIC (Supplementary Fig. 6). Furthermore, subregional trends indicate that the changes in regional MLD, chl-*a* and Δp_{CO_2} are primarily driven by changes in the south subregion (Supplementary Table 1). Here, the effect on $p_{CO_{2,sur}}$ from a large increase in biological DIC drawdown is more than twice that of an increase in anthropogenic DIC (Supplementary Fig. 6), resulting in a large significant decrease in Δp_{CO_2} (−4.6 µatm yr^{-1}, $P = 0.005$; Supplementary Table 1), which is more than twice the magnitude of the atmospheric CO_2 trend. The increases in regional and subregional biological DIC drawdown are consistent with the increases in chl-*a* (Fig. 4b and Supplementary Table 1), underscoring the critical role of phytoplankton in driving Δp_{CO_2}. These results demonstrate that from 1993 to 2017 during summer along the mid/southern WAP, changes in sea ice dynamics drove an increase in upper ocean stability, which drove an increase in phytoplankton biomass and biological DIC drawdown, resulting in greater oceanic CO_2 uptake.

The increase in regional phytoplankton biomass (Fig. 4b) raises the possibility that micronutrients like iron could eventually limit biological production and oceanic CO_2 uptake during summer along the mid/southern WAP. Surface iron shows a cross-shore gradient, with higher concentrations towards the coast, and is supplied by remnant winter water in combination with sea ice melt on the slope and outer shelf, and with meteoric (glacial meltwater and precipitation), sub-glacial and sedimentary sources towards the coast[26,27]. It is predicted that the SAM will remain positive, with strong winds persisting and temperatures continuing to increase along the WAP, resulting in further glacial retreat and sea ice decline[11]. In the short term, it is possible that surface iron levels could increase under these conditions[26], allowing a continued increase in phytoplankton biomass. However, even with no change in biological production, a continued increase in upper ocean stability could drive a continued increase in oceanic CO_2 uptake through enhanced biological volumetric DIC drawdown (Fig. 3).

In the long term, it has been demonstrated that the effects of climate change are progressing southward along the WAP, given the substantial declines in sea ice, upper ocean stability, phytoplankton biomass and diatom proportion along the northern WAP[20]. Our results demonstrate the progression of these effects into the mid/southern WAP, and their impact on upper ocean physics and biogeochemistry. Here, there have been smaller (larger) increases

in upper ocean stability, phytoplankton biomass, biological DIC drawdown and oceanic CO_2 uptake in the north (south) subregion (Supplementary Table 1 and Supplementary Fig. 6). The meridional variability in these changes in phytoplankton biomass, biological DIC drawdown and oceanic CO_2 uptake are associated with shifts in phytoplankton community composition, as there has been a relatively larger increase in cryptophytes (diatoms) in the north (south) subregion (Supplementary Table 1). In this study, we demonstrate strong coupling between upper ocean physics and biogeochemistry during summer along the mid/southern WAP (Figs. 2–4). As sea ice further declines to critical levels here, a decrease in upper ocean stability could drive a decrease in phytoplankton biomass and biological DIC drawdown, negatively impacting oceanic CO_2 uptake during summer. This could be compounded by a further shift from diatoms to cryptophytes. A decline in sea ice could also lead to a diminished 'rectification' of the seasonal CO_2 air–sea flux cycle[38], resulting in enhanced outgassing during other seasons, although the ultimate impact of increased air–sea exchange and continued rising atmospheric CO_2 concentrations on net annual oceanic CO_2 uptake is uncertain[39]. Our analysis is possible due to the sustained and consistent spatio-temporal sampling of coincident physical and biogeochemical oceanographic variables during summer along the mid/southern WAP by the Palmer LTER and DPT programmes, which should be expanded to other seasons and sites around Antarctica. In the coming decades, it is predicted that sea ice will decline around much of the continent[11]. Therefore, despite a recent increase, the future of the WAP, and other Antarctic coastal regions, may be as a reduced sink for atmospheric CO_2.

Online content

Any methods, additional references, Nature Research reporting summaries, source data, statements of code and data availability and associated accession codes are available at https://doi.org/10.1038/s41558-019-0552-3.

Received: 29 November 2018; Accepted: 9 July 2019;
Published online: 26 August 2019

References

1. Sabine, C. L. et al. The oceanic sink for anthropogenic CO_2. *Science* **305**, 367–371 (2004).
2. Takahashi, T. et al. The changing carbon cycle in the Southern Ocean. *Oceanography* **25**, 26–37 (2012).
3. McKinley, G. A., Fay, A. R., Lovenduski, N. S. & Pilcher, D. J. Natural variability and anthropogenic trends in the ocean carbon sink. *Annu. Rev. Mar. Sci.* **9**, 125–150 (2017).
4. Gruber, N., Landschützer, P. & Lovenduski, N. S. The variable Southern Ocean carbon sink. *Annu. Rev. Mar. Sci.* **11**, 159–186 (2019).
5. Schofield, O. et al. How do polar marine ecosystems respond to rapid climate change? *Science* **328**, 1520–1523 (2010).
6. Takahashi, T. et al. Global sea-air CO_2 flux based on climatological surface ocean p_{CO_2}, and seasonal biological and temperature effects. *Deep Sea Res. Pt II* **49**, 1601–1622 (2002).
7. Schofield, O. et al. Changes in the upper ocean mixed layer and phytoplankton productivity along the West Antarctic Peninsula. *Phil. Trans. R. Soc. Lond. A* **376**, 20170173 (2018).
8. Fay, A. R., McKinley, G. A. & Lovenduski, N. S. Southern Ocean carbon trends: sensitivity to methods. *Geophys. Res. Lett.* **41**, 6833–6840 (2014).
9. Lovenduski, N. S., Fay, A. R. & McKinley, G. A. Southern Ocean CO_2 uptake: what can we learn from an ocean model? *Glob. Biogeochem. Cycles* **29**, 416–426 (2015).
10. Munro, D. R. et al. Recent evidence for a strengthening CO_2 sink in the Southern Ocean from carbonate system measurements in the Drake Passage (2002–2015). *Geophys. Res. Lett.* **42**, 7623–7630 (2015).
11. Turner, J. et al. Antarctic climate change and the environment: an update. *Polar Rec.* **50**, 237–259 (2014).
12. Martinson, D. G., Stammerjohn, S. E., Iannuzzi, R. A., Smith, R. C. & Vernet, M. Western Antarctic Peninsula physical oceanography and spatio-temporal variability. *Deep Sea Res. Pt II* **55**, 1964–1987 (2008).
13. Meredith, M. P. & King, J. C. Rapid climate change in the ocean west of the Antarctic Peninsula during the second half of the 20th century. *Geophys. Res. Lett.* **32**, L19604 (2005).
14. Cook, A. J., Fox, A. J., Vaughan, D. G. & Ferrigno, J. G. Retreating glacier fronts on the Antarctic Peninsula over the past half-century. *Science* **308**, 541–544 (2005).
15. Stammerjohn, S. E., Martinson, D. G., Smith, R. C. & Iannuzzi, R. A. Sea ice in the western Antarctic Peninsula region: spatio-temporal variability from ecological and climate change perspectives. *Deep Sea Res. Pt II* **55**, 2041–2058 (2008).
16. Thompson, D. W. & Solomon, S. Interpretation of recent Southern Hemisphere climate change. *Science* **296**, 895–899 (2002).
17. Marshall, G. J. Trends in the Southern Annular Mode from observations and reanalyses. *J. Clim.* **16**, 4134–4143 (2003).
18. Stammerjohn, S. E., Martinson, D. G., Smith, R. C., Yuan, X. & Rind, D. Trends in Antarctic annual sea ice retreat and advance and their relation to El Niño–Southern oscillation and Southern Annular Mode variability. *J. Geophys. Res. Oceans* **113**, C03S90 (2008).
19. Ducklow, H. W. et al. West Antarctic Peninsula: an ice-dependent coastal marine ecosystem in transition. *Oceanography* **26**, 190–203 (2013).
20. Montes-Hugo, M. et al. Recent changes in phytoplankton communities associated with rapid regional climate change along the western Antarctic Peninsula. *Science* **323**, 1470–1473 (2009).
21. Meredith et al. Changing distributions of sea ice melt and meteoric water west of the Antarctic Peninsula. *Deep Sea Res. Pt II* **139**, 40–57 (2017).
22. Kim, H. et al. Climate forcing for dynamics of dissolved inorganic nutrients at Palmer Station, Antarctica: an interdecadal (1993–2013) analysis. *J. Geophys. Res. Biogeosci.* **121**, 2369–2389 (2016).
23. Carvalho, F., Kohut, J., Oliver, M. J., Sherrell, R. M. & Schofield, O. Mixing and phytoplankton dynamics in a submarine canyon in the West Antarctic Peninsula. *J. Geophys. Res. Oceans* **121**, 5069–5083 (2016).
24. Saba, G. K. et al. Winter and spring controls on the summer food web of the coastal West Antarctic Peninsula. *Nat. Commun.* **5**, 4318 (2014).
25. Vernet, M. et al. Primary production within the sea-ice zone west of the Antarctic Peninsula: I – Sea ice, summer mixed layer, and irradiance. *Deep Sea Res. Pt II* **55**, 2068–2085 (2008).
26. Annett, A. L. et al. Controls on dissolved and particulate iron distributions in surface waters of the western Antarctic Peninsula shelf. *Mar. Chem.* **196**, 81–97 (2017).
27. Sherrell, R. M. et al. A 'shallow bathtub ring' of local sedimentary iron input maintains the Palmer deep biological hotspot on the West Antarctic Peninsula shelf. *Phil. Trans. R. Soc. Lond. A* **376**, 20170171 (2018).
28. Carrillo, C. J., Smith, R. C. & Karl, D. M. Processes regulating oxygen and carbon dioxide in surface waters west of the Antarctic Peninsula. *Mar. Chem.* **84**, 161–179 (2004).
29. Eveleth, R., Cassar, N., Doney, S. C., Munro, D. R. & Sweeney, C. Biological and physical controls on O_2/Ar, Ar and p_{CO_2} variability at the western Antarctic Peninsula and in the Drake Passage. *Deep Sea Res. Pt II* **139**, 77–88 (2017).
30. Hauri, C. et al. Two decades of inorganic carbon dynamics along the West Antarctic Peninsula. *Biogeosciences* **12**, 6761–6779 (2015).
31. Ito, R. G., Tavano, V. M., Mendes, C. R. B. & Garcia, C. A. E. Sea-air CO_2 fluxes and p_{CO_2} variability in the northern Antarctic Peninsula during three summer periods (2008-2010). *Deep Sea Res. Pt II* **149**, 84–98 (2018).
32. Legge, O. J. et al. The seasonal cycle of carbonate system processes in Ryder Bay, West Antarctic Peninsula. *Deep Sea Res. Pt II* **139**, 167–180 (2017).
33. Tortell, P. D. et al. Metabolic balance of coastal Antarctic waters revealed by autonomous p_{CO_2} and ΔO_2/Ar measurements. *Geophys. Res. Lett.* **41**, 6803–6810 (2014).
34. Schofield, O. et al. Decadal variability in coastal phytoplankton community composition in a changing West Antarctic Peninsula. *Deep Sea Res. Pt I* **124**, 42–54 (2017).
35. Haberman, K. L., Ross, R. M. & Quetin, L. B. Diet of the Antarctic krill (*Euphausia superba* Dana): II. Selective grazing in mixed phytoplankton assemblages. *J. Exp. Mar. Biol. Ecol.* **283**, 97–113 (2003).
36. Stoecker, D. K., Hansen, P. J., Caron, D. A. & Mitra, A. Mixotrophy in the marine plankton. *Annu. Rev. Mar. Sci.* **9**, 311–335 (2017).
37. Moline, M. A., Claustre, H., Frazer, T. K., Schofield, O. & Vernet, M. Alteration of the food web along the Antarctic Peninsula in response to a regional warming trend. *Glob. Change Biol.* **10**, 1973–1980 (2004).
38. Yager, P. L. et al. The northeast water polynya as an atmospheric CO_2 sink: a seasonal rectification hypothesis. *J. Geophys. Res. Oceans* **100**, 4389–4398 (1995).
39. Sweeney, C. in *Biogeochemistry of the Ross Sea* Vol. 78 (eds Ditullio, G. R. & Dunbar, R. B.) 295–312 (American Geophysical Union, 2003).

Acknowledgements

We thank all past and present members of the Palmer LTER for their dedication in the field and laboratory. Additionally, we thank all past and present support crew for their assistance. This paper benefitted from comments provided by R. Sherrell, S. Stammerjohn and T. Takahashi. This research was supported by NSF Office of Polar Programs Integrated Systems Science Program Award No. 1440435 to H.W.D. and O.M.S. for the Palmer LTER, NSF Office of Polar Programs Award No. 1543457 to D.R.M. and C.S. for the DPT and NSF Office of Polar Programs Award No. 1501997 to C.S. for additional support. This is Palmer LTER Contribution No. 622.

Author contributions

M.S.B. and O.M.S. conceived the study. M.S.B. analysed the data and wrote the manuscript. C.S. and D.R.M. provided the DPT p_{CO_2} dataset. C.J.F. and D.R.M. provided valuable data interpretation and synthesis. H.W.D. led the Palmer LTER programme. All authors reviewed and edited the manuscript.

Competing interests

The authors declare no competing interests.

Additional information

Supplementary information is available for this paper at https://doi.org/10.1038/s41558-019-0552-3.

Reprints and permissions information is available at www.nature.com/reprints.

Correspondence and requests for materials should be addressed to M.S.B.

Peer review information: *Nature Climate Change* thanks Nicolas Metzl and the other, anonymous, reviewer(s) for their contribution to the peer review of this work.

Publisher's note: Springer Nature remains neutral with regard to jurisdictional claims in published maps and institutional affiliations.

Methods

Palmer LTER. Data for this study were collected over 25 years during the Palmer LTER programme annual regional research cruises conducted each austral summer month of January from 1993 to 2017 (1993–1997 aboard the MV *Polar Duke*; 1998–2017 aboard the ARSV *Laurence M. Gould*) along the mid/southern WAP. The Palmer LTER regional sampling grid spans from Palmer Station in the north to Charcot Island in the south and from the coast to the slope (Fig. 1b)[19]. The regional sampling grid consists of grid lines 100 km apart that lie perpendicular to the WAP coastline, with sampling stations located 20 km apart from the coast to the slope (Fig. 1b)[40]. From 1993 to 2008, primarily lines 600 to 200 were sampled, although line 100 also was sampled in 2007 and 2008. In 2009, the grid was expanded to the south to include lines 000 to −100, with reduced sampling further north. We divide the Palmer LTER regional sampling grid into nine subregions, including the north (lines 600 to 400), south (lines 300 to 200), far south (lines 100 to −100), slope, shelf and coast (Fig. 1b)[12,15].

Water column physics and stability. Water column temperature (T; °C) and salinity (S; PSU) as a function of pressure (p; dbar) was measured with a SeaBird 911+ CTD. Data were quality-controlled by removal of observations with values outside realistic environmental ranges (T: −2–4 °C; S: 30–42 PSU). Seawater thermodynamic calculations were performed with the Gibbs-SeaWater Oceanographic Toolbox for MATLAB (v.3.06)[41]. For each CTD cast, profiles of conservative temperature (T_c; °C) were calculated from T, and profiles of absolute salinity (S_a; PSU) were calculated from S. Using p, T_c and S_a, profiles of density (ρ; kg m^{-3}), potential density referenced to 0 dbar (ρ_0; kg m^{-3}) and buoyancy frequency squared (N^2; s^{-2}) were calculated. To define an ecologically relevant MLD (m) an approach based on maximum N^2 was used[42]. For each CTD cast, MLD was determined as the depth of maximum N^2. Identification of a MLD assumes the existence of a stratified ocean consisting of a homogeneous upper ocean layer overlying a relatively more heterogeneous layer. To test the validity of this assumption, for each CTD cast, a quality index (QI; dimensionless; 0–1) was calculated based on the ratio of the standard deviation of ρ_0 in the MLD to that over a deeper portion of the water column[43]. The QI facilitated characterization of MLDs determined with certainty (QI ≥ 0.8), some uncertainty (0.5 ≤ QI < 0.8), or not at all (QI < 0.5). Only MLDs with a QI ≥ 0.5 were included in this study (75% of CTD casts).

For each CTD cast, surface averages of T, S and ρ were calculated by averaging any observations between 0 and 5m, the approximate depth of the ship's surface seawater flow-through system intake. Water column T and S were also recorded with the DIC and TA observations (see below), using either the corresponding CTD cast or the ship's surface seawater flow-through system. Additionally, continuous observations of surface T and S were made from 2003 to 2017 using the ARSV *Laurence M. Gould* surface seawater flow-through system as part of the DPT programme. These T and S data were quality-controlled, used to calculate ρ and used to calculate surface averages of T, S and ρ in the same manner as the CTD casts. The DPT S data for the years 2003 and 2004 were anomalously high and were excluded. A merged surface $T/S/\rho$ dataset was constructed by combining the CTD and DPT surface data. Unless specifically stated, this dataset was used for all analyses involving surface $T/S/\rho$.

Water column discrete sampling. Water column samples for phytoplankton pigments and dissolved inorganic variables were drawn from Niskin bottles deployed at depth or from the ship's surface seawater flow-through system at underway stations. The concentration of chl-*a* (mg m^{-3}) was measured with fluorescence[44]. From 1993 to 2008, samples for chl-*a* via fluorescence were size-fractionated. Only the >0.45 µm, or if missing, the (>0.45 µm and ≤20 µm) + (>20 µm) size fractions were considered in this study. From 2009 to 2017, GF/F filters (0.70 µm) were used for data collection. The concentration of phytoplankton accessory pigments and chl-*a* (all mg m^{-3}) were measured with HPLC, using GF/F filters for data collection. Phytoplankton chemotaxonomy (group proportion of total chl-*a*; dimensionless; 0–1) was determined with CHEMTAX (v.1.95) using initial pigment ratios derived for the WAP[45]. The groups resolved included diatoms, cryptophytes, mixed flagellates (small dinoflagellates and unidentified phytoflagellates), prasinophytes and type-4 haptophytes (*Phaeocystis* spp.). Multiplication of group proportion by total chl-*a* yielded group chl-*a*. In the Palmer LTER database, prasinophytes and type-4 haptophytes rarely contribute substantially to surface community biomass (that is representing ≥50% of total chl-*a*) and were excluded from further analyses. Phytoplankton chemotaxonomy data were excluded for observations where chl-*a* was zero or missing, or fucoxanthin, alloxanthin or 19′-butanoyloxyfucoxanthin (the primary diatom, cryptophyte and mixed flagellate chemotaxonomic pigments, respectively) were missing. This quality-control step resulted in the exclusion of phytoplankton chemotaxonomy data for all observations from the year 2000 due to the absence of alloxanthin. Two parallel chl-*a* via HPLC datasets were generated, which included either: (1) all observations (used for time series), or (2) only observations with corresponding accessory pigment data (used for chemotaxonomy). HPLC data were missing for the years 2002, 2010 and 2012 due to instrument or freezer failures, and were not yet available for 2017.

DIC (µmol kg^{-1}) was measured by coulometric analysis. TA (µequiv. kg^{-1}) was measured by potentiometric titration. Sample collection, handling and analysis for DIC and TA was performed according to WOCE-JGOFS protocols[46], using certified reference materials provided by A. Dickson (Scripps Institute of Oceanography), with a measurement precision of ±2 µmol kg^{-1} and ±5 µequiv. kg^{-1}, respectively[30]. Samples for DIC and TA, from the same sample bottle preserved with 200 µl of saturated $HgCl_2$, were typically analysed within 6 months of collection at the University of Hawaii (1993–2002), Virginia Institute of Marine Science (2003–2007), the Marine Biological Laboratory (2008–2013), or Lamont-Doherty Earth Observatory (2014–2017). DIC measurements were corrected for the $HgCl_2$ addition with a dilution factor. Any DIC or TA observation pseudoreplicates were averaged. TA data were missing for the years 2003 and 2004. Concentrations of dissolved inorganic macronutrients, including nitrate, nitrite, phosphate and silicate (all µmol l^{-1}), were measured by continuous flow analysers. Depending on the study year, the nitrate/nitrite dataset was reported as either: (1) just nitrate, (2) just nitrate + nitrite, or (3) nitrate, nitrite and nitrate + nitrite. Given that nitrite is typically low relative to nitrate[22], a continuous nitrate + nitrite dataset (henceforth nitrate) was constructed using the nitrate + nitrite data, or if missing and nitrate was present, the sum of nitrate and nitrite. Phosphate data were missing for the year 1997, and all macronutrient data were missing for 1998.

Observations with ambiguous time, event number, latitude/longitude, or depth metadata were excluded. Data were quality-controlled by removal of observations with values outside of realistic environmental ranges (chl-*a*: 0–60 mg m^{-3}; DIC: 1800–2300 µmol kg^{-1}; TA: 2000–2500 µequiv. kg^{-1}; nitrate: 0–50 µmol l^{-1}; phosphate: 0–5 µmol l^{-1}; silicate: 0–175 µmol l^{-1}). Replicate observations per depth were averaged. Surface averages of all variables were calculated by averaging observations between 0 and 5 m, the approximate depth of the ship's surface seawater flow-through system intake. Surface averages of phytoplankton group proportion were computed as the ratio of surface group chl-*a* to surface total chl-*a*. Surface averages of salinity-normalized DIC (sDIC; µmol kg^{-1}) and TA (sTA; µequiv. kg^{-1}) were computed using a reference value of 33.4 PSU (the historic average of all single-station bins). For each surface DIC and TA observation, if either surface T or S was not recorded, they were calculated from any of the merged surface $T/S/\rho$ dataset observations within the nearest single-station bin, or if either of these was missing, the nearest double-station bin, weighted by their inverse distance to the DIC and TA observation (Fig. 1b). Surface averages of nitrate, phosphate and silicate were converted to units of µmol kg^{-1} using surface ρ. For each macronutrient observation, surface S and ρ were calculated from any of the merged surface $T/S/\rho$ dataset observations within the nearest single station bin, or if either was missing, the nearest double-station bin, weighted by their inverse distance to the macronutrient observation (Fig. 1b). Surface averages of salinity-normalized nitrate, phosphate and silicate were calculated as above for sDIC and sTA.

Observation and estimation of $p_{CO_{2,sur}}$ and Δp_{CO_2}. Continuous observations of $p_{CO_{2,sur}}$ (µatm) were made from 2003 to 2017 using a 30 l shower-type air–water equilibrator and infrared CO_2 analyser integrated into the ARSV *Laurence M. Gould* surface seawater flow-through system as part of the DPT programme according to ref. [47] ($p_{CO_{2,sur,DPT}}$; µatm). Data for the year 2016 were not present in the Surface Ocean CO_2 Atlas (v6) (SOCAT)[48] dataset and therefore were excluded. Discrete estimates of $p_{CO_{2,sur}}$ were made from 1993 to 2017 using the surface averages of Palmer LTER DIC, TA, T, S, phosphate and silicate with CO2SYS for MATLAB (v.1.1)[49] using dissociation constants for carbonic acid provided by ref. [50] ($p_{CO_{2,sur,LTER}}$; µatm). For each DIC observation missing a paired TA observation, TA was estimated (TA_{est}; µequiv. kg^{-1}) from S according to: $TA_{est} = 57.01S + 373.86$, as described in ref. [30]. If either surface T or S were not recorded, they were calculated from the merged surface $T/S/\rho$ dataset as described above. Values for surface phosphate and silicate were calculated in the same way, or if missing, from the climatology of the nearest double-station bin (Fig. 1b).

The relationship between $p_{CO_{2,sur,LTER}}$ and $p_{CO_{2,sur,DPT}}$ was assessed with a match-up analysis. For each $p_{CO_{2,sur,LTER}}$ observation, any $p_{CO_{2,sur,DPT}}$ observations within 1 day and 1 km were averaged ($p_{CO_{2,sur,DPT,match}}$; µatm). Any values of $p_{CO_{2,sur,LTER}}$ or $p_{CO_{2,sur,DPT,match}}$ less (greater) than the 0.5th (99.5th) percentiles of $p_{CO_{2,sur,DPT,match}}$ were removed. A major-axis type-II linear regression model was then constructed between $p_{CO_{2,sur,LTER}}$ and $p_{CO_{2,sur,DPT,match}}$ using MATLAB (Supplementary Fig. 7). This regression model was used to estimate $p_{CO_{2,sur,DPT}}$ from $p_{CO_{2,sur,LTER}}$ ($p_{CO_{2,sur,DPT,est}}$; µatm).

Measurements of $p_{CO_{2,atm}}$ (µatm) were made using atmospheric pressure (mbar) and the dry air mole fraction of CO_2 in the atmosphere ($x_{CO_{2,atm}}$; ppm). For the DPT observations, $p_{CO_{2,atm}}$ ($p_{CO_{2,atm,DPT}}$; µatm) used atmospheric pressure from the ARSV *Laurence M. Gould*. For the LTER observations, $p_{CO_{2,atm}}$ ($p_{CO_{2,atm,LTER}}$; µatm) used atmospheric pressure from Palmer Station. For both the DPT and LTER observations, $x_{CO_{2,atm}}$ was determined at the ship location using the NOAA Earth System Research Laboratory Greenhouse Gas Marine Boundary Layer Reference[51]. Measurements of Δp_{CO_2} (µatm) were made by subtracting

$p_{CO_{2,atm}}$ from $p_{CO_{2,sur}}$. For the DPT observations, Δp_{CO_2} ($\Delta p_{CO_{2,DPT}}$; µatm) was determined by subtracting $p_{CO_{2,atm,DPT}}$ from $p_{CO_{2,sur,DPT}}$. For the LTER observations, Δp_{CO_2} ($\Delta p_{CO_{2,DPT,est}}$; µatm) was determined by subtracting $p_{CO_{2,atm,LTER}}$ from $p_{CO_{2,sur,DPT,est}}$. The 1993–2017 $p_{CO_{2,sur}}$ and Δp_{CO_2} datasets used for this study were constructed by merging $p_{CO_{2,sur,DPT,est}}$ and $\Delta p_{CO_{2,DPT,est}}$ for 1993–2002 and 2016 with $p_{CO_{2,sur,DPT}}$ and $\Delta p_{CO_{2,DPT}}$ for 2003–2015 and 2017.

Modelling of Δp_{CO_2}. The relationship between Δp_{CO_2} and MLD given a constant rate of biological production was modelled (Fig. 3). A winter water DIC (DIC_{ww}; µmol kg^{-1}) value of 2180 µmol kg^{-1} was determined based on the analysis of ref. [30]. A seasonally integrated (from November to January) net community production (NCP_{ndj}; mol C m^{-2}) value of 1.3 mol C m^{-2}, integrated to the MLD, was determined by estimating an average seasonal daily NCP value of 30 mmol O_2 m^{-2} day^{-1} from ref. [52], converting to units of C using a photosynthetic quotient of 1.4 and assuming 60 days of NCP prior to observation by the Palmer LTER annual regional research cruise during summer. A summer surface ρ (ρ_{su}; kg m^{-3}) value of 1027 kg m^{-3} was determined from the historic average of all single-station bins (Fig. 1b). For each MLD spanning 1 to 120 m, the corresponding seasonal DIC drawdown (DIC_{dd}; µmol kg^{-1}) was computed according to: $DIC_{dd} = ((NCP_{ndj})(10^6))/((\rho_{su})(MLD))$, and summer surface DIC was computed by subtracting DIC_{dd} from DIC_{ww}. Next, summer surface TA, *T*, *S*, phosphate and silicate values of 2283 µequiv. kg^{-1}, 1 °C, 33.4 PSU, 1 µmol kg^{-1} and 53 µmol kg^{-1}, respectively, were determined from the historic average of all single-station bins (Fig. 1b). For each MLD, summer $p_{CO_{2,sur}}$ was calculated using the summer surface DIC, TA, *T*, *S*, phosphate and silicate values with CO2SYS for MATLAB (v.1.1)[49] using dissociation constants for carbonic acid provided by ref. [50], and summer Δp_{CO_2} was calculated by subtracting a $p_{CO_{2,atm}}$ value of 365 µatm (the 1993–2017 average) from summer $p_{CO_{2,sur}}$.

Drivers of $p_{CO_{2,sur}}$. Following the approach of previous authors[10,53], growth rates of $p_{CO_{2,sur}}$ drivers, including surface *T*, *S*, DIC and TA, were calculated and converted into units of $p_{CO_{2,sur}}$ using the approximations of ref. [54,55] (Supplementary Tables 1 and 2 and Supplementary Fig. 6). Revelle factors of 15 and −15 for DIC and TA, respectively, were used based on approximations presented by ref. [56]. Additionally, following the approach of ref. [57], growth rates of sDIC and sTA were calculated and converted into units of $p_{CO_{2,sur}}$ to separate the indirect influence of a long-term change in *S* through DIC and TA on $p_{CO_{2,sur}}$. The growth rate in $p_{CO_{2,sur}}$ due to sDIC was further divided into components due to long-term changes in both biological DIC drawdown and anthropogenic DIC. An estimate of 0.79 ± 0.16 µmol kg^{-1} yr^{-1} was used for the trend in anthropogenic DIC, based on the reported anthropogenic DIC increase of 12–18 µmol kg^{-1} over 19 years in Antarctic Surface Water[58], derived from repeat hydrography observations from 1992 to 2011 along line S04P (see also fig. 5c in ref. [58]). Time series trends and averages used in this analysis are presented in Supplementary Tables 1 and 2.

Statistics. Surface data were binned to different spatial scales depending on the analysis. For each year, data were spatially averaged into 100 km × 20 km (along-shore × cross-shore) bins encompassing a single Palmer LTER regional sampling grid station, that is single-station bins (Fig. 1b). This facilitated the direct comparison of different variables (Figs. 2a and 3 and Supplementary Figs. 3–5). Single-station bins of phytoplankton group proportion were computed as the ratio of average group chl-*a* to average total chl-*a*. The single-station chl-*a* via fluorescence and HPLC data were $\log_{10}$-transformed for normality. To account for rare zero values, a small offset (~10% of the minimum non-zero value) was first added to the chl-*a* via HPLC data. Unless noted, analyses were performed on the $\log_{10}$-transformed chl-*a* via fluorescence and HPLC data. Due to a large number of zero values, the single-station group chl-*a* data were not $\log_{10}$-transformed (zero values of group proportion yielded zero values of group chl-*a*). Given that each station is not visited every year, for each year, the single-station bins were spatially averaged into 100 km × 40 km (along-shore × cross-shore) bins encompassing two Palmer LTER regional sampling grid stations, that is double-station bins (Fig. 1b). For the chl-*a* via fluorescence, Δp_{CO_2} and MLD climatologies (Fig. 2b,c and Supplementary Fig. 1), only double-station bins with observations for at least one-third of the time series were included (9 and 3 years for the north/south and far south subregions, respectively). To compare yearly subregional (slope, shelf and coast subregions) chl-*a* via fluorescence and Δp_{CO_2} (Fig. 2d), for each year, the corresponding single-station bins were spatially averaged.

To construct regional and subregional (north and south subregions) time series (Fig. 4, Supplementary Tables 1 and 2 and Supplementary Fig. 6), the 16 double-station bins encompassing the Palmer LTER regional sampling grid stations used by ref. [7] that are typically visited each year were used (Fig. 1b). Regional time series used all 16 bins, and subregional time series used the corresponding nine or seven (north or south subregion) bins. For each year, the median and 25th and 75th percentiles of the bins were calculated. The median was used to reduce skew in the regional and subregional estimates due to any extreme values and strong cross-shore patterns.

To examine the relationship between chl-*a* via fluorescence and Δp_{CO_2} (Fig. 2a,d), two-sided Spearman's rhos were calculated using MATLAB. To determine temporal trends in regional and subregional time series, type I linear regression models were constructed between variables and study year using MATLAB (Fig. 4, Supplementary Table 1 and Supplementary Fig. 6). To examine differences in chl-*a* via HPLC, Δp_{CO_2}, MLD, *T*, *S*, sDIC and salinity-normalized nitrate and phosphate between diatom, cryptophyte and mixed flagellate assemblages (Supplementary Figs. 3–5), Kruskal-Wallis tests and post-hoc pairwise multiple comparisons with a Bonferroni adjustment were performed using Statistica. This is a nonparametric test. Diatom, cryptophyte and mixed flagellate assemblages were functionally defined as observations with group chl-*a* ≥ 75% of total chl-*a*. The locations of diatom, cryptophyte and mixed flagellate assemblages observed from 1993 to 2017 are shown in Supplementary Fig. 2. All three groups are observed on the slope, shelf and coast. However, diatoms occur more frequently than the other groups on the slope and in the far south, as they often bloom along the ice edge and earlier in the season (summer conditions occur later further south)[34].

Reporting Summary. Further information on research design is available in the Nature Research Reporting Summary linked to this article.

Data availability

The Palmer LTER dataset, sampling and analysis protocols and Palmer Station atmospheric pressure dataset can be accessed at http://pal.lternet.edu. The DPT p_{CO_2} dataset can be accessed at https://www.socat.info/. The NOAA ESRL Greenhouse Gas Marine Boundary Layer Reference can be accessed at https://www.esrl.noaa.gov/gmd/ccgg/mbl/data.php. Figs. 2–4, Supplementary Tables 1 and 2 and Supplementary Figs. 1–7 present data from the above datasets.

Code availability

The custom MATLAB (R2018a) code written to read and analyse data and generate figures is fully available on request from the corresponding author.

References

40. Waters, K. J. & Smith, R. C. Palmer LTER: a sampling grid for the palmer LTER program. *Antarct. J. US* **27**, 236–239 (1992).
41. McDougall, T. J. & Barker, P. M. *Getting Started with TEOS-10 and the Gibbs Seawater (GSW) Oceanographic Toolbox* (SCOR/IAPSO WG127, 2011).
42. Carvalho, F., Kohut, J., Oliver, M. J. & Schofield, O. Defining the ecologically relevant mixed-layer depth for Antarctica's coastal seas. *Geophys. Res. Lett.* **44**, 338–345 (2017).
43. Lorbacher, K., Dommenget, D., Niiler, P. P. & Köhl, A. Ocean mixed layer depth: a subsurface proxy of ocean-atmosphere variability. *J. Geophys. Res. Oceans* **111**, C07010 (2006).
44. Parsons, R. T., Maita, Y. & Lalli, C. M. *A Manual of Chemical and Biological Methods for Seawater Analysis* (Pergammon, 1984).
45. Kozlowski, W. A., Deutschman, D., Garibotti, I., Trees, C. & Vernet, M. An evaluation of the application of CHEMTAX to Antarctic coastal pigment data. *Deep Sea Res. Pt I* **58**, 350–364 (2011).
46. Dickson, A. G. & Goyet, C. *Handbook of Methods for the Analysis of the Various Parameters of the Carbon Dioxide System in Sea Water Version 2* ORNL/CDIAC-74 (Oak Ridge National Laboratory, 1994).
47. Munro, D. R. et al. Estimates of net community production in the Southern Ocean determined from time series observations (2002-2011) of nutrients, dissolved inorganic carbon, and surface ocean p_{CO_2} in Drake Passage. *Deep Sea Res. Pt II* **114**, 49–63 (2015).
48. Bakker et al. A multi-decade record of high-quality fCO_2 data in version 3 of the surface ocean CO_2 atlas (SOCAT). *Earth Syst. Sci. Data* **8**, 383–413 (2016).
49. van Heuven, S., Pierrot, D., Rae, J. W. B., Lewis, E. & Wallace, D. W. R. *MATLAB Program Developed for CO_2 System Calculations* ORNL/CDIAC-105b (Oak Ridge National Laboratory, 2011).
50. Lueker, T. J., Dickson, A. G. & Keeling, C. D. Ocean p_{CO_2} calculated from dissolved inorganic carbon, alkalinity, and equations for K_1 and K_2: validation based on laboratory measurements of CO_2 in gas and seawater at equilibrium. *Mar. Chem.* **70**, 105–119 (2000).
51. Dlugokencky, E. J., Thoning, K. W., Lang, P. M. & Tans, P. M. *NOAA Greenhouse Gas Reference from Atmospheric Carbon Dioxide Dry Air Mole Fractions from the NOAA ESRL Carbon Cycle Cooperative Global Air Sampling Network* (NOAA, 2017); ftp://aftp.cmdl.noaa.gov/data/trace_gases/co2/flask/surface/
52. Li, Z., Cassar, N., Huang, K., Ducklow, H. & Schofield, O. Interannual variability in net community production at the Western Antarctic Peninsula region (1997–2014). *J. Geophys. Res. Oceans* **121**, 4748–4762 (2016).

53. Lenton, A. et al. The observed evolution of oceanic p_{CO_2} and its drivers over the last two decades. *Glob. Biogeochem. Cycles* **26**, GB2021 (2012).
54. Takahashi, T., Olafsson, J., Goddard, J. G., Chipman, D. W. & Sutherland, S. C. Seasonal variation of CO_2 and nutrients in the high-latitude surface oceans: a comparative study. *Glob. Biogeochem. Cycles* **7**, 843–878 (1993).
55. Takahashi, T. et al. Climatological distributions of pH, p_{CO_2}, total CO_2, alkalinity, and $CaCO_3$ saturation in the global surface ocean, and temporal changes at selected locations. *Mar. Chem.* **164**, 95–125 (2014).
56. Sarmiento, J. L. & Gruber, N. *Ocean Biogeochemical Dynamics* (Princeton Univ. Press, 2006).
57. Lovenduski, N. S., Gruber, N., Doney, S. C. & Lima, I. D. Enhanced CO_2 outgassing in the southern ocean from a positive phase of the Southern Annular Mode. *Glob. Biogeochem. Cycles* **21**, GB2026 (2007).
58. Williams, N. L. et al. Quantifying anthropogenic carbon inventory changes in the Pacific sector of the Southern Ocean. *Mar. Chem.* **174**, 147–160 (2015).

nature research

Corresponding author(s): Michael S. Brown

Reporting Summary

Nature Research wishes to improve the reproducibility of the work that we publish. This form provides structure for consistency and transparency in reporting. For further information on Nature Research policies, see Authors & Referees and the Editorial Policy Checklist.

Statistical parameters

When statistical analyses are reported, confirm that the following items are present in the relevant location (e.g. figure legend, table legend, main text, or Methods section).

n/a	Confirmed	
☐	☒	The exact sample size (*n*) for each experimental group/condition, given as a discrete number and unit of measurement
☒	☐	An indication of whether measurements were taken from distinct samples or whether the same sample was measured repeatedly
☐	☒	The statistical test(s) used AND whether they are one- or two-sided *Only common tests should be described solely by name; describe more complex techniques in the Methods section.*
☒	☐	A description of all covariates tested
☐	☒	A description of any assumptions or corrections, such as tests of normality and adjustment for multiple comparisons
☐	☒	A full description of the statistics including central tendency (e.g. means) or other basic estimates (e.g. regression coefficient) AND variation (e.g. standard deviation) or associated estimates of uncertainty (e.g. confidence intervals)
☐	☒	For null hypothesis testing, the test statistic (e.g. *F*, *t*, *r*) with confidence intervals, effect sizes, degrees of freedom and *P* value noted *Give P values as exact values whenever suitable.*
☒	☐	For Bayesian analysis, information on the choice of priors and Markov chain Monte Carlo settings
☒	☐	For hierarchical and complex designs, identification of the appropriate level for tests and full reporting of outcomes
☐	☒	Estimates of effect sizes (e.g. Cohen's *d*, Pearson's *r*), indicating how they were calculated
☐	☒	Clearly defined error bars *State explicitly what error bars represent (e.g. SD, SE, CI)*

Our web collection on statistics for biologists may be useful.

Software and code

Policy information about availability of computer code

Data collection	No software was used. The data was retrieved from publicly available datasets.
Data analysis	Custom MATLAB (R2018a) code was written to read and analyze data and generate figures, and is fully available upon request. Seawater thermodynamic calculations were performed with the Gibbs-SeaWater Oceanographic Toolbox for MATLAB (v3.06). Phytoplankton chemotaxonomy was determined with CHEMTAX (v1.95). Seawater carbonate system calculations were made with with CO2SYS for MATLAB (v1.1).

For manuscripts utilizing custom algorithms or software that are central to the research but not yet described in published literature, software must be made available to editors/reviewers upon request. We strongly encourage code deposition in a community repository (e.g. GitHub). See the Nature Research guidelines for submitting code & software for further information.

Data

Policy information about availability of data

All manuscripts must include a data availability statement. This statement should provide the following information, where applicable:

- Accession codes, unique identifiers, or web links for publicly available datasets
- A list of figures that have associated raw data
- A description of any restrictions on data availability

The Palmer LTER dataset, sampling and analysis protocols and Palmer Station atmospheric pressure dataset can be accessed at http://pal.lternet.edu. The DPT pCO2 dataset can be accessed at https://www.socat.info/. The NOAA ESRL Greenhouse Gas Marine Boundary Layer Reference can be accessed at https://www.esrl.noaa.gov/gmd/ccgg/mbl/data.php. Figs. 2–4, Supplementary Tables 1 and 2 and Supplementary Figs. 1–7 present data from the above datasets.

Field-specific reporting

Please select the best fit for your research. If you are not sure, read the appropriate sections before making your selection.

☐ Life sciences ☐ Behavioural & social sciences ☒ Ecological, evolutionary & environmental sciences

For a reference copy of the document with all sections, see nature.com/authors/policies/ReportingSummary-flat.pdf

Ecological, evolutionary & environmental sciences study design

All studies must disclose on these points even when the disclosure is negative.

Study description	This study is an analysis of long-term observational ecological data collected by the Palmer Long-Term Ecological Research and Drake Passage Time-Series programs.
Research sample	This study uses long-term observational ecological data, consisting of measurements of seawater physical properties, phytoplankton pigments, and seawater carbonate system variables and inorganic nutrients. The data were collected by the Palmer Long-Term Ecological Research and Drake Passage Time-Series programs.
Sampling strategy	The Palmer Long-Term Ecological Research program's regional sampling grid covers a representative region of the West Antarctic Peninsula marine ecosystem. The grid spans from Palmer Station in the north to Charcot Island in the south, and from the coast to the continental slope. The grid consists of grid lines 100 km apart that lie perpendicular to the coast with sampling stations located 20 km apart from the coast to the continental slope, which together allow sufficient regional sampling. The annual regional research cruises are conducted during the austral summer month of January, which is the period of maximum biological activity.
Data collection	Data for this study were collected and recorded over 25 years by experienced research groups of the Palmer Long-Term Ecological Research program.
Timing and spatial scale	Data for this study were collected during the Palmer Long-Term Ecological Research program's annual regional research cruises, conducted each austral summer month of January from 1993 to 2017 along the West Antarctic Peninsula.
Data exclusions	Observations with ambiguous time, event number, latitude/longitude, or depth metadata were excluded. Data were quality-controlled by excluding any observations with values outside of realistic environmental ranges.
Reproducibility	This study uses long-term observational ecological data, with no experimental manipulation. To ensure reproducibility, data were retrieved from publicly available datasets.
Randomization	This study uses long-term observational ecological data, with no experimental manipulation. To determine differences in water mass properties between phytoplankton groups, data were limited to where groups contributed at least 75% of phytoplankton biomass.
Blinding	This study uses long-term observational ecological data, with no experimental manipulation.

Did the study involve field work? ☒ Yes ☐ No

Field work, collection and transport

Field conditions	The data were retrieved from publicly available datasets.
Location	Sampling was conducted within the Palmer Long-Term Ecological Research program's regional sampling grid along the West Antarctic Peninsula, centered at approximately 67 deg. S, 70 deg. W. Surface samples were primarily used (at most 5 m), although seawater physical properties were measured throughout the water column to determine upper ocean stability.
Access and import/export	The data were retrieved from publicly available datasets.
Disturbance	The data were retrieved from publicly available datasets.

Reporting for specific materials, systems and methods

Materials & experimental systems		Methods	
n/a	Involved in the study	n/a	Involved in the study
☒	☐ Unique biological materials	☒	☐ ChIP-seq
☒	☐ Antibodies	☒	☐ Flow cytometry
☒	☐ Eukaryotic cell lines	☒	☐ MRI-based neuroimaging
☒	☐ Palaeontology		
☐	☒ Animals and other organisms		
☒	☐ Human research participants		

Animals and other organisms

Policy information about studies involving animals; ARRIVE guidelines recommended for reporting animal research

Laboratory animals	This study did not involve laboratory animals.
Wild animals	This study did not involve wild animals.
Field-collected samples	Seawater samples were collected in the field and filtered in the lab for the collection of phytoplankton biomass, which was immediately frozen for the later quantification of phytoplankton pigments in the lab.